Broadband enhanced backscattering spectroscopy of strongly scattering media

O. L. Muskens, A. Lagendijk

Center for Nanophotonics, FOM Institute for Atomic and Molecular Physics AMOLF, Kruislaan 407, 1098 SJ Amsterdam, The Netherlands

muskens@amolf.nl

Abstract: We report on a new experimental method for enhanced backscattering spectroscopy (EBS) of strongly scattering media over a bandwidth from 530-1000 nm. The instrument consists of a supercontinuum light source and an angle-dependent detection system using a fiber-coupled grating spectrometer. Using a combination of two setups, the backscattered intensity is obtained over a large angular range and using circularly polarized light. We present broadband EBS of a TiO_2 powder and of a strongly scattering porous GaP layer. In combination with theoretical model fits, the EBS system yields the optical transport mean free path over the available spectral window.

OCIS codes: (160.4236) Nanomaterials; (290.4210) Multiple scattering; (300.6250) Spectroscopy, condensed matter; (350.4238) Nanophotonics and photonic crystals

References and links

1. M. P. van Albada and A. Lagendijk, 'Observation of Weak Localization of Light in a Random Medium,' Phys. Rev. Lett. **55**, 2692 (1985)
2. P.-E. Wolf and G. Maret, 'Weak Localization and Coherent Backscattering of Photons in Disordered Media,' Phys. Rev. Lett. **55**, 2696 (1985)
3. R. Vreeker, M. P. van Albada, R. Sprik, and A. Lagendijk, 'Femtosecond time-resolved measurements of weak localization of light,', Phys. Lett. A, **132**, 51 (1988)
4. K. M. Yoo, K. Arya, G. C. Tang, J. L. Birman, and R. R. Alfano, 'Coherent backscattering of a picosecond pulse from a disordered medium: Analysis of the pulse shape in the time domain,' Phys. Rev. A **39**, 3728 (1989)
5. Y. L. Kim, Y. Liu, V. M. Turzhitsky, H. K. Roy, R. K. Wali, and V. Backman, 'Coherent backscattering spectroscopy,' Opt. Lett. **29**, 1906 (2004)
6. Y. L. Kim, Y. Liu,R. K. Wali, H. K. Roy, and V. Backman, 'Low-coherent backscattering spectroscopy for tissue characterization,' Appl. Opt. **44**, 366 (2007)
7. A. A. Chabanov and A. Z. Genack, 'Photon localization in resonant media,' Phys. Rev. Lett. **87**, 153901 (2001)
8. M. Reufer, L. F. Rojas-Ochoa, S. Eiden, J. J. Sáenz, and F. Scheffold, 'Transport of light in amorphous photonic materials,' Appl. Phys. Lett. **91**, 171904 (2007)
9. A.F. Koenderink, M. Megens, G. van Soest, W.L. Vos, and A. Lagendijk, 'Enhanced backscattering from photonic crystals,' Phys. Lett. A. **268**, 104 (2000)
10. D.S. Wiersma, M.P. van Albada, and A. Lagendijk, 'An accurate technique to record the angular distribution of backscattered light,' Rev. Sci. Instr. **66**, 5473 (1995)
11. P. Gross, M. Störzer, S. Fiebig, M. Clausen, G. Maret, and C. M. Aegerter, 'A Precise method to determine the angular distribution of backscattered light to high angles,' Rev. Sc. Instr. **78**, 033105 (2007)
12. R. H. J. Kop, P. de Vries, R. Sprik, and A. Lagendijk, 'Observation of anomolous transport of strongly multiple scattered light in thin disordered samples,' Phys. Rev. Lett. **79**, 4369 (1997)
13. I. M. Vellekoop, P. Lodahl, and A. Lagendijk, 'Determination of the diffusion constant using phase-sensitive measurements,' Phys. Rev. E **71**, 056604 (2005)

14. P. Lodahl and A. Lagendijk, 'Transport of quantum noise through random media,' Phys. Rev. Lett. **94**, 153905 (2005)
15. A. Lagendijk, R. Vreeker, and P. de Vries, 'Influence of internal reflection on diffusive transport in strongly scattering media,' Phys. Lett. A **136**, 81 (1989)
16. J. X. Zhu, D. J. Pine, and D. A. Weitz, 'Internal reflection of diffusive light in random media,' Phys. Rev. A **44**, 3948 (1991)
17. M. U. Vera and D. J. Durian, 'Angular distribution of diffusely transmitted light,' Phys. Rev. B **53**, 3215 (1996)
18. F.J.P. Schuurmans, D. Vanmaekelbergh, J. van de Lagemaat, and A. Lagendijk, 'Strongly Photonic Macroporous GaP Networks,' Science **284**, 141 (1999)
19. F.J.P. Schuurmans, M. Megens, D. Vanmaekelbergh, and A. Lagendijk, 'Light scattering near the localization transition in macroporous GaP networks,' Phys. Rev. Lett. **83**, 2183 (1999)
20. P. M. Johnson, A. Imhof, B. P. J. Bret, J. Gómez Rivas, and A. Lagendijk, 'Time-resolved pulse propagation in a strongly scattering material,' Phys. Rev. E 68, 016604:1-9 (2003)
21. B. A. van Tiggelen, D. A. Wiersma, and A. Lagendijk, 'Self-consistent theory for the enhancement factor in coherent backscattering,' Eur. Phys. Lett. **30**, 1 (1995)
22. S. Fiebig, C.M. Aegerter, W. Bührer, M. Störzer, E. Akkermans, G. Montambaux, and G. Maret, 'Conservation of energy in coherent backscattering of light,' cond-mat/0706.0381 (2007).
23. M. B. van der Mark, M. P. van Albada, and A. Lagendijk, 'Light scattering in strongly scattering media: Multiple scattering and weak localization,' Phys. Rev. B **37**, 3575 (1988)

1. Introduction

Transport of light in random photonic media is governed by an interplay of diffusion and interference. Even in weakly scattering media, interference of multiple scattering optical paths gives rise to weak localization (enhanced backscattering) of light [1, 2]. Ever since its first discovery, enhanced backscattering spectroscopy (EBS) has been recognized as an important tool for investigating the photonic strength of multiple scattering media. EBS is traditionally performed at a fixed optical frequency using a coherent light source such as a laser. Since EBS involves interference of reciprocal light paths of equal length, temporal coherence of the impinging light does not affect the shape of the EBS-cone in time-independent measurements. In time-resolved experiments, short light pulses have been used to investigate the optical path length distribution in EBS [3, 4].

Enhanced backscattering using a broadband, low spatial-coherence source has recently been employed for depth-resolved profiling of biological tissue [5]. With low-spatial coherence light, optical paths with a transverse distance at the surface larger than the spatial coherence length do not contribute to enhanced backscattering. This spatial coherence can be increased by reducing the size of the light source, allowing in principle the studies of long light paths using a normal Xe-lamp [6]. However, for the strongly photonic materials of interest in many of the multiple-scattering experiments, the large angular width of the EBS cone combined with the low spectral power density of conventional light sources has limited the use of spectrally resolved EBS. Broadband EBS would be an especially valuable technique as it could provide a simultaneous characterization of strongly photonic media over a wide frequency range. Such spectral information is of importance for instance in investigating the transition regime close to Anderson localization, since it in principle allows observation both the non-localized and localized regime in one single realization of disorder [7]. Further, spectrally resolved experiments reveal important properties of a medium which are hard to assess from single-wavelength experiments, such as resonant scattering [8] or photonic bandgaps [9].

Here, we present a new technique employing a supercontinuum light source for spectrally-resolved enhanced backscattering over a large optical bandwidth from 530 nm to 1000 nm. This novel approach has been enabled by the very high spectral stability of modern integrated supercontinuum fiber sources, allowing for long acquisition times with low drift. The high spatial coherence of the source is defined by the collimated output of a single-mode photonic crystal fiber. The setup presented here has several advantages with respect to other implementations

of enhanced backscattering [10, 11]. The off-centered rotation technique [10] is limited to an angular range of several tens of degrees, while the presence of a beamsplitter limits the use of circular polarization channels. A CCD or detector-array approach [11] facilitates very precise alignment, and is required when the EBS cone should be captured instantaneously, e.g. in dynamic light-scattering experiments. In case of spectral imaging over a wide angular range, the scanning configuration presented here is advantageous since it provides both the backscattering and diffuse transfer functions over 360° without normalization to an asymmetric [10] or detector-dependent [11] instrumental response. Furthermore, circular polarization channels can be used with better than 99% suppression of orthogonal helicity channels over the entire angular and spectral range. The technique is especially suited for very strongly scattering media near $k\ell = 1$, $k = 2\pi/\lambda$ and ℓ being the optical wavevector and the transport mean free path, respectively, where the EBS-cone spans a large angular range.

2. Setup

For the experimental determination of the enhanced backscattering cone we make use of an angle-dependent light scattering setup combining two configurations. These are (i) a large-angle scanning configuration using a 3-mm prism reflector and (ii) a small-angle configuration around the backscattering direction using a semitransparent beamsplitter to couple in the light. Figure 1(a) presents a side-view of experimental configuration (i) for large-angle scattering. A fiber laser (Fianium SC-450-2) produces a broadband spectrum spanning the visible and infrared with a total power of 2 W via supercontinuum generation in a photonic crystal fiber. The output of the fiber is collimated and filtered by means of a broadband linear polarization filter. The optical beam is directed onto the scattering medium using a 3-mm, Al-coated, inverted prism, positioned at a distance of 25 cm from the sample. The angular range which is blocked by the shadow of the prism in this configuration amounts to $\pm 0.8^\circ$ around the backscattering angle. A range of scattering wavevectors of 0.3° is selected by means of a diaphragm, after which the light is filtered using an analyzing polarization filter and focused onto a 600 μm multimode fiber connected to a spectrometer with a resolution of 0.7 nm (Ocean Optics USB4000). The detection optics is mounted on a rotating arm which allows scanning over 360° in the horizontal plane. To avoid contributions of the polarization dependent response of the fiber spectrometer, a third polarizer is placed in front of the detection fiber at a fixed polarization angle of 45° with respect to the two orthogonal (*s*- and *p*-) analyzer states. Individual spectra are collected over an integration time of 500 ms per measurement. To cover the important angular range around the exact backscattering direction, the setup is converted to configuration (ii) [c.f. Fig. 1(b)], in which the prism is replaced by a beamsplitter while maintaining the same optical beam path. In this configuration a scanning range from -7° to 7° is available. Scattering emerging from the light path transmitted through the beamsplitter is suppressed by a beam dump. In all experiments, the sample surface is centered at the point of rotation by optimizing the collected intensity at the angles of $\pm 85^\circ$.

An important but spurious factor in enhanced backscattering spectroscopy is single scattering. Single scattering does not have a distinct time reversed path and therefore does not contribute to the EBS cone. It gives however rise to a background intensity which reduces the coherent backscattering enhancement factor. Further, since the single scattering differential cross-section can be highly nonisotropic depending on the geometry of the scatterers, which may distort the shape of the EBS cone. To eliminate contributions of single scattering, we employ its helicity nonconserving property to separate it from the helicity conserving EBS cone. For this purpose, achromatic MgF_2/quartz $\lambda/4$ waveplates are added in the setup. In configuration (i), two separate $\lambda/4$ waveplates are used in the incident and scattered beam paths since the prism reflector does not modify the polarization state of the light. Thus, angular scanning

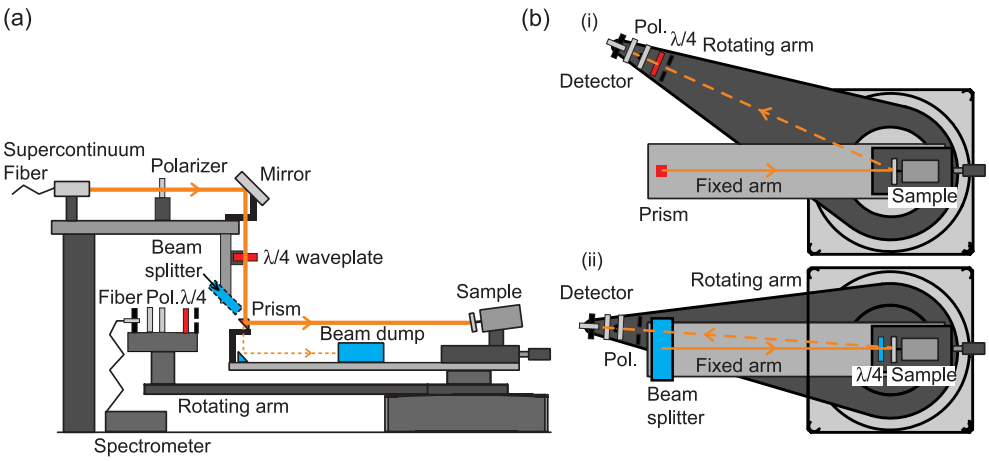

Fig. 1. Schematic overview of experimental setup for broadband enhanced backscattering spectroscopy using a supercontinuum source and a fiber spectrometer. The two configurations (i) and (ii) can be obtained by replacing the 3-mm right-angle prism reflector by a beamsplitter. For experiments using circular polarized light, the two separate $\lambda/4$ waveplates in (i) are replaced by a single $\lambda/4$ waveplate directly in front of the sample in (ii). In configuration (ii) the light transmitted by the beamsplitter is collected by a beam dump.

over 360° range is possible while preserving circular polarization selectivity better than 10^2. As the response of the beamsplitter in configuration (ii) is strongly polarization dependent, in this configuration a single $\lambda/4$ waveplate is placed directly in front of the sample.

3. Enhanced backscattering spectra of TiO_2 powder

The spectrally resolved backscattering was measured from a slab of TiO_2 powder of 18.1μm thickness. This specific sample has been used in several studies and is well characterized by means of total transmission and time-resolved diffusion experiments [12, 13, 14]. In order to properly normalize the coherent backscattering cone to the angle-dependent diffuse background, often a turbid material with a very long transport mean free-path is used as a reference [10, 11]. This approach implicitly assumes that the diffuse angular reflection functions of both the material under study and the reference medium are the same. However, the diffuse angular transmission and reflection from a scattering medium are strongly influenced by reflection of light at its interface, which depends both on the effective refractive index and on surface roughness [15, 16, 17].

To investigate the effect of various normalizations on the EBS cone, we measured the diffuse angular reflection functions $P(\mu)/\mu$ [17], where μ is the cosine of the backscattering angle $\mu = \cos(\theta)$, for the TiO_2 layer as well as for a 1 cm thick piece of teflon. The results for $P(\mu)/\mu$, at a wavelength λ of 700 nm are shown in Fig. 2(a) against μ for several conditions. Firstly, the helicity conserving channel of TiO_2 (black line), containing the EBS cone at $\mu > 0.95$, is compared with the helicity nonconserving channel of TiO_2 (green line) and with the helicity conserving channel of teflon (blue line). To correct for differences in albedo between the two samples, the teflon function was scaled vertically to those of TiO_2 at $\mu = 0.1$. Clearly, the diffuse reflectivity from the helicity nonconserving channel of TiO_2 and from the helicity conserving channel of teflon do not coincide for $\mu > 0.5$. The helicity nonconserving channel contains the class of single scattering events, which for finite scatterers may give rise to a non-isotropic background. For linearly polarized light, single scattering is polarization conserving.

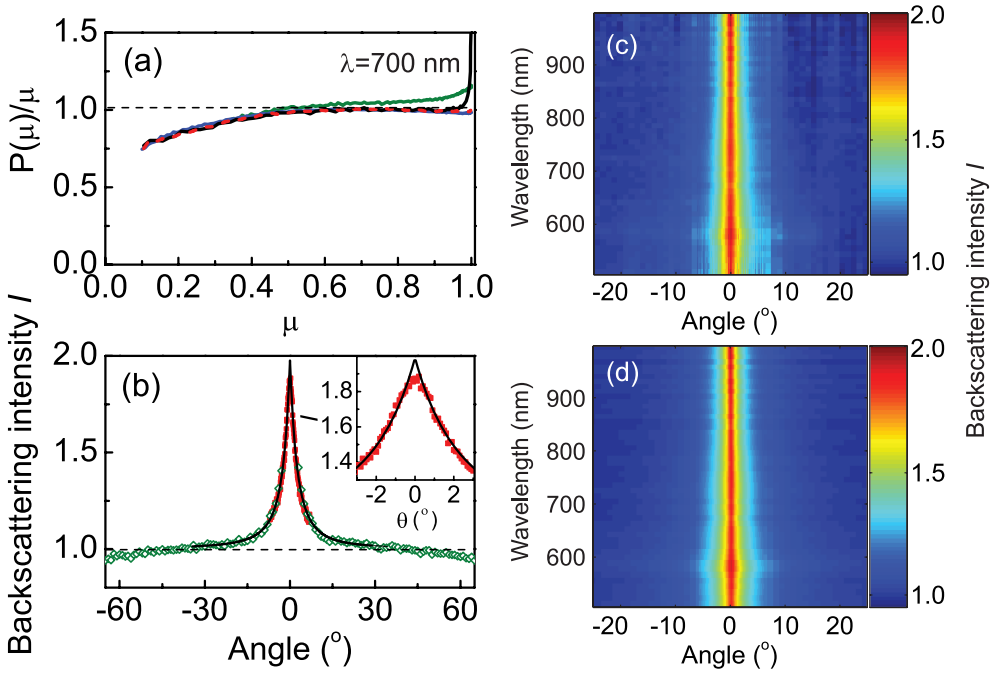

Fig. 2. (color online) (a) Diffuse angular transmission function $P(\mu)/\mu$ against $\mu = \cos(\theta)$ in backscattering, at $\lambda = 700$ nm, for (black line) TiO_2 and (blue line) teflon, both helicity conserving channel, (green line) TiO_2 helicity nonconserving channel, and (dashed red line) TiO_2 linear-polarization nonconserving channel (averaged over *s* and *p* output polarizations). (b) EBS of TiO_2 sample at $\lambda = 700$ nm, normalized to linear-polarization nonconserving channel of TiO_2, measured using configuration (i) (open diamonds, green) and configuration (ii) (squares, red), and fit using Eq. (2) (black line). Inset: detail of (b) around cone center. (c) Color density plot showing enhanced backscattering intensity from the TiO_2 powder sample over a wavelength range of 520-1000 nm. (d) Same for fitted EBS cones using Eq. (2).

Therefore, we measured the diffuse angular reflection function in the linear-polarization nonconserving channel for both the *s* and *p*-polarizations. The average of these two measurements is shown by the red dashed line in Fig. 2(a). The measurement of the linear-polarization nonconserving channel of TiO_2 coincides well with that of the helicity conserving channel of teflon for all μ, and follows the diffuse background of the helicity conserving channel of TiO_2 up to $\mu = 0.95$. This correspondence can be explained by the close resemblance of the effective index of refraction of the TiO_2 layer ($n_{\text{eff}} \simeq 1.34$) and that of teflon (n = 1.34).

In the following, we normalized the scattered intensity in the helicity conserving channel to that in the linear-polarization nonconserving channel to obtain the EBS cone. The result at $\lambda = 700$ nm is shown by the red dots in Fig. 2(b), where the experimental data points from the large-angle setup (open diamonds, green) have been combined with the small-angle setup (open squares, red). The normalized intensities of the large- and small-angle configurations are overlayed and a small amplitude factor ($< 10\%$), due to a systematic shift in alignment, is corrected using the average intensities in the overlapping regions. Finally, the EBS measurements are normalized to unity at an angle of -30°, i.e. next to the wings of the EBS-cone, for each wavelength. Figure 2(c) shows a color density plot of the EBS spectra over the wavelength range from 530-1000 nm. The width of the EBS profiles varies slightly over the selected spec-

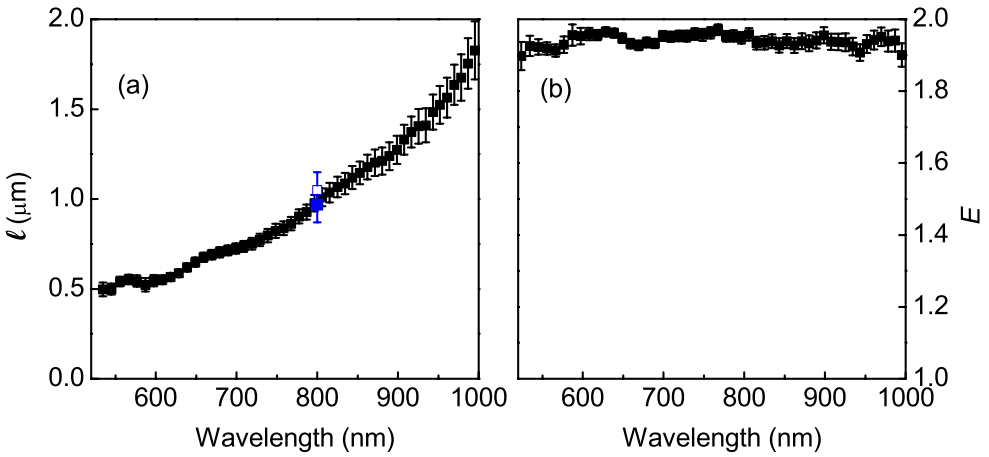

Fig. 3. Fitted values of (a) the transport mean free path ℓ and (b) the enhancement factor E as a function of wavelength, for the TiO_2 powder sample (circles, black). Previously reported measurements on the same sample are indicated from (blue square) Refs. [12, 13] and (open blue square) Ref. [14], both at $\lambda = 780$ nm.

tral window, indicating that the photonic strength $1/(k\ell)$ of the TiO_2 powder is only weakly dependent on wavelength. To extract the wavelength dispersion of the mean free path, the EBS cone was fitted at each wavelength independently using a new set of equations describing enhanced backscattering, which improve significantly on existing models in literature. The effect of finite reflectivity at the interface has been taken into account using the method of mirror images weighted by the Fresnel coefficient, which, following the approach of Ref. [15], gives the Green function F for the semi-infinite medium

$$F(z_1,z_2,\mathbf{q}_\perp) = G_d(z_1-z_2,\mathbf{q}_\perp) + \frac{z_e q_\perp - 1}{z_e q_\perp + 1} G_d(z_1+z_2,\mathbf{q}_\perp), \tag{1}$$

where z_e denotes the extrapolation length, $q_\perp = k_0 \sin\theta$ denotes the momentum transfer between incoming and outgoing wavevectors parallel to the surface, and G_d is the diffusion Green function for an infinite medium, $G_d(z,\mathbf{q}_\perp) = \exp(-zq_\perp)/(2q_\perp)$. Using this Green function, the angle-dependent enhanced backscattering, $I(\theta)$, normalized to the diffuse background, can be written as

$$I(\theta) = [\gamma_\ell + (E-1)\gamma_c]/\gamma_\ell, \tag{2}$$

where E denotes the experimental enhancement factor, which may deviate from the ideal factor of two due to residual single scattering and stray background radiation. The bistatic coefficients γ_ℓ and γ_c denote the contributions of the ladder and maximally crossed diagrams in the diffusion approximation, respectively, given by

$$\begin{aligned} \gamma_\ell &= 3\mu\left(\tau_e + \frac{\mu\mu_i}{\mu+\mu_i}\right) \\ \gamma_c &= \frac{3}{2\mu_i \nu}\frac{1}{(\alpha+\nu)^2+u^2}\left(1+\frac{2\nu\tau_e}{1+\tau_e\alpha}\right), \end{aligned} \tag{3}$$

where the abbreviations $\tau_e = z_e/\ell$, $\alpha = q_\perp \ell$, $u = k_0\ell(\mu_i - \mu)$, and $\nu = \frac{1}{2}(1/\mu + 1/\mu_i)$ have been introduced, $\mu_i = \cos\theta_i$ being the cosine of the incident angle ($\mu_i \simeq 1$). The EBS cones were fitted at each wavelength over an angular range from -30 ° to 30° using as free parameters

the scattering mean free path ℓ and the enhancement factor E. The extrapolation length of the sample was determined by total transmission experiments as $z_e/\ell = 1.76 \pm 0.1$ [12]. The wavelength dependence of this factor can be considered as a second order correction and is therefore not taken into account in this study.

The fitted EBS cones are shown as a color density plot in Fig. 2(d), a cross-section at 700 nm wavelength is represented by the black line in Fig. 2(b). In the fit we have excluded a $\pm 0.5^\circ$ region around the center to avoid effects of cone rounding in the experimental data. The fitted EBS cone shapes agree well with the measured ones (residuals less than 5% between 650-800 nm). The measured cone shows a less pronounced cusp at exact backscattering than the calculation because of the limited resolution of the setup and partly due to the finite size of the sample ($L/\ell_{700} \simeq 25$). The limited resolution also contributes to the reduction of the enhancement factor E below two. The fitting results for the free parameters ℓ and E are shown against wavelength in Fig. 3(a,b). The error bars represent the 95% confidence interval obtained from the residuals of the fit. A smooth variation of the parameters is observed, with $E > 1.9$ indicating a good reduction of single scattering at all wavelengths. The mean free path ℓ increases from $\ell_{530} = 0.49 \pm 0.03$ μm at 530 nm to $\ell_{1000} = 1.6 \pm 0.1$ μm at 1000 nm, corresponding to a change in $k_0\ell$ from 5.8 ± 0.4 to 10.4 ± 0.8. Previous results for ℓ on the same sample, obtained using total transmission experiments, are indicated by the open blue squares in Fig. 3(a) [12, 13, 14]. Our results at the wavelength of 780 nm correspond to these values within experimental uncertainty.

4. Porous gallium phosphide

Porous gallium phosphide (PA-GaP), obtained by photoanodical etching of a crystalline GaP wafer, is to date the most strongly scattering medium in the visible range [18]. We have measured the broadband EBS of this material using the same procedure as described in Sec. 3. The diffuse angular reflectance functions $P(\mu)/\mu$ are shown in Fig. 4(a), again for the helicity conserving channels of PA-GaP (black line) and teflon (blue line), the helicity nonconserving channel of PA-GaP (green line), and the linear-polarization nonconserving channel of PA-GaP (dashed red line). For teflon, the diffuse reflection function considerably differs from those of PA-GaP. This difference can be attributed to the large effective refractive index of the PA-GaP layer, $n_{\text{eff}} = 1.7 \pm 0.1$, resulting in an angle- and polarization-averaged internal reflection coefficient $\overline{R}$ (c.f. Ref. [17]) of 0.67 for PA-GaP versus 0.44 for teflon. The helicity nonconserving channel of PA-GaP layer [green line in Fig. 4(a)] contains single scattering, therefore the linear-polarization nonconserving channel (red dashed line) again gives the best reference for the diffusive background.

The resulting EBS cones are plotted in Fig. 4(b), where we have shown both the intensity normalized to either the linear-polarization nonconserving channel of PA-GaP (green and red symbols), and to the helicity conserving channel of the teflon reference (blue line). Both cones are normalized to unity at -30°, i.e. in the far wing of the cone. The EBS normalized to teflon clearly contains a slope in the background resulting from the difference in the diffuse angular reflectance functions of teflon and PA-GaP. The teflon-normalized cone has in a full width-at-half maximum of 7.8°. The cone normalized to the linear-polarization nonconserving channel has a slightly narrower width of 6.7°. It also shows a much flatter background, with a slight undercut which may result from energy conservation in enhanced backscattering [21, 22]. However, we find that the far wings of the cone are strongly affected by small misalignments in the positioning of the sample at the center of rotation, resulting in either a slight undercut, as in Fig. 4(b), or a small positive slope, as in Fig. 2(b). We will not analyze this effect further at this point, but rather focus on the angular range containing the EBS-cone.

The experimental and fitted spectral maps of the enhanced backscattering in PA-GaP are

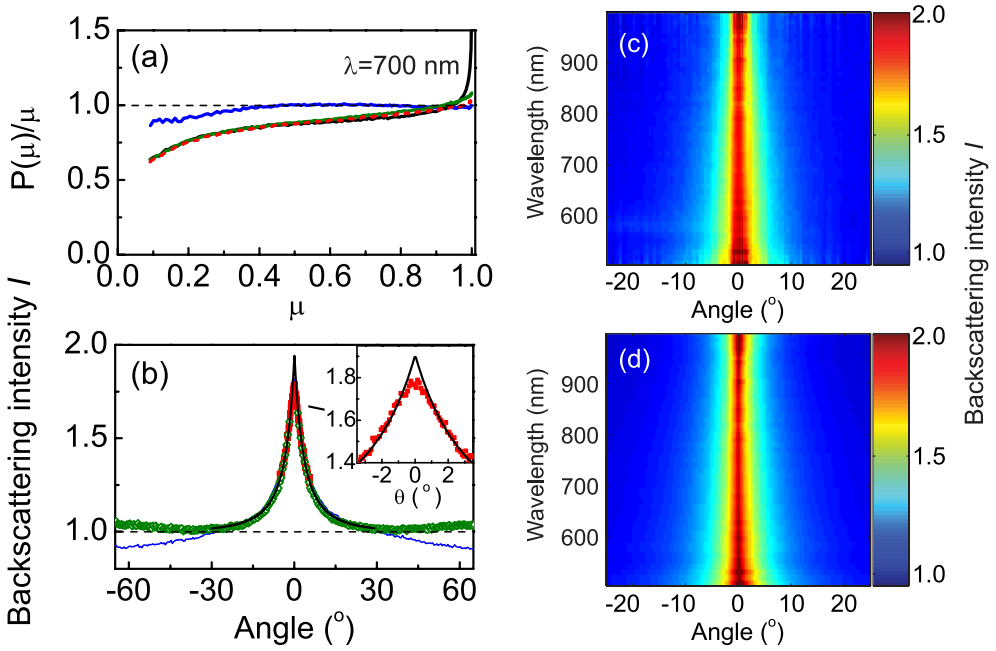

Fig. 4. (a) Diffuse angular transmission function $P(\mu)/\mu$ against $\mu = \cos(\theta)$ in backscattering, at $\lambda = 700$ nm, for (black line) PA-GaP and (blue line) teflon, both helicity conserving channel, (green line) PA-GaP helicity nonconserving channel, and (dashed red line) PA-GaP linear polarization nonconserving channel, averaged over *s* and *p* output polarizations. (b) EBS of PA-GaP sample at $\lambda = 700$ nm, normalized to linear-polarization nonconserving channel of PA-GaP, for large-angle configuration (i) (open squares, green) and small-angle configuration (ii) (diamonds, red), and EBS normalized to the teflon diffuse angular reflectance function (blue line). Black line is a fit using Eq. (2). Inset: detail of (b) around cone center. (c) Color density plot showing enhanced backscattering intensity from the TiO_2 powder sample over a wavelength range of 520-1000 nm. (d) Fitted enhanced backscattering cones using Eq. (2).

shown as color density plots in Fig. 4(c,d), with a cross section at $\lambda = 700$ nm in Fig. 4(b) (black line). In the fits, an extrapolation length of $z_e/\ell = 3.5$, obtained from total transmission experiments, has been used [19]. Good agreement is again obtained in the shape of the EBS cones except for a deviation in the cusp at the center [see inset Fig. 4(b)]. An anomalous rounding of the cone has been reported earlier on the same sample [19], which has been attributed to a suppression of long light paths in the layer due to localization. A detailed investigation of this rounding requires a much higher angular resolution than currently available, which is therefore beyond the scope of our investigation.

The fitted values for the mean free path ℓ and enhancement factor E are shown in Fig. 5(a,b). The mean free path varies from $\ell_{530} = 0.20 \pm 0.05\ \mu$m at $\lambda = 530$ nm to $\ell_{1000} = 0.75 \pm 0.1\ \mu$m at $\lambda = 1000$ nm, corresponding to an increase of $k_0\ell$ from 2.4 ± 0.3 up to 4.7 ± 0.6. A significant difference is found between the fitted values of l obtained from the broadband EBS and earlier measurements on the same sample, as indicated by the open blue symbols in Fig. 5(a) [18, 19, 20]. Several of these earlier measurements were done using total transmission [18, 20]. In those investigations it has been observed that, due to the electrochemical etching process used in the preparation of the samples, a top layer with a different morphology is present. Since EBS is more sensitive to this modified top layer, whereas total transmission probes mainly the bulk of

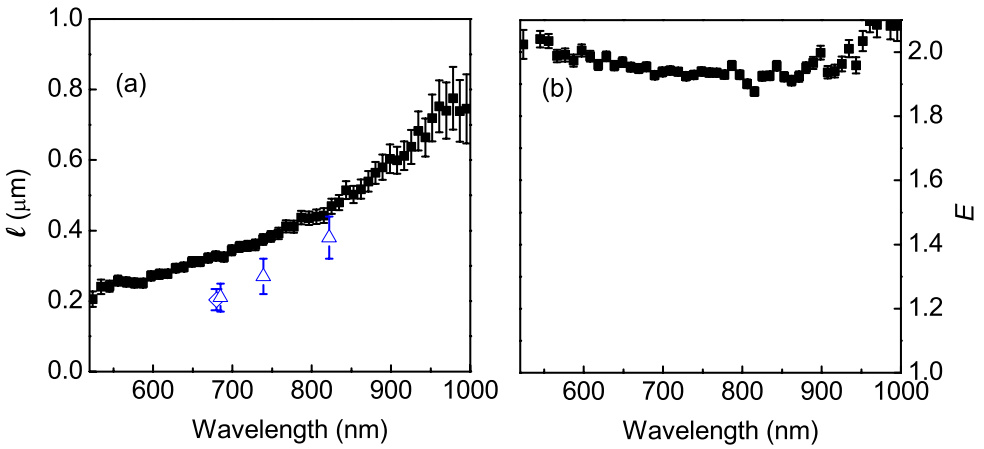

Fig. 5. Fitted values of (a) the transport mean free path l and (b) the enhancement factor E as a function of wavelength, for a 25.5-μm thick PA-GaP slab, normalized to the diffuse angular reflectance in the linear-polarization nonconserving channel (squares, black). Symbols denote previously reported measurements from Refs. [18, 19] (open blue diamond) and [20] (open blue triangles).

the porous layer for thick slabs, we believe that the difference in measured ℓ can be explained by the different morphology of the surface and bulk regions of the PA-GaP.

However, Schuurmans et al. [19] reported a similar small value of ℓ from EBS as from total transmission. The discrepancy with our current investigation can be explained by two independent differences in the analysis. Firstly, the use of teflon as a reference for the diffuse scattering background accounts for a difference of 16% in cone width. Secondly, the original models describing the EBS cone including internal reflections [16, 23] are incomplete. Specifically, the widely-used formula $k_0\ell = 0.7/\theta_{\mathrm{FWHM}}(1-\overline{R})$, with θ_{FWHM} the angular full width-at-half maximum of the cone, breaks down for $\overline{R}$ approaching unity. The improved model, as presented in Eqs. (1-3), includes internal reflection in a more correct way by including the fresnel factor in the semi-infinite Green function Eq. (1), which is valid for all values of $\overline{R}$. For the relatively large value of $\overline{R} = 0.67$ for PA-GaP, the mean free paths obtained from the current model are approximately 30% higher than from the previous models. We emphasize that the main conclusions of Ref. [19] do not depend on the exact value of the mean free path. Also we point out that in recent literature, models incorporating internal reflection in an incomplete way are still frequently being used to determine the scattering strength. For materials with large extrapolation length z_e this will in general result in an overestimate of the photonic strength $1/(k\ell)$.

Altogether, we believe that the new determination of ℓ is representative for the top layer of the PA-GaP and is not in conflict with earlier measurements using total transmission. Both old and new measurement are consistent in the variation of the mean free path with wavelength, indicating that the photonic strength of the PA-GaP layer is strongly dependent on wavelength. We do not observe any resonances in the mean free path, as expected from the broad distribution of pore sizes and the strongly correlated network of scatterers.

5. Conclusions

In conclusion, we have demonstrated a broadband enhanced backscattering method which allows simultaneous acquisition of EBS cones over a wide spectral range. This method will find use in fundamental and applied science as a tool in characterizing the nanoscale morphology of

scattering media by their wavelength-dependent photonic strength. Especially in the search for Anderson localization in 3D media the method will find use in optimizing the spectral region of interest and discriminating regimes of (resonant) strong multiple scattering near $k\ell \sim 1$. We find that broadband supercontinuum radiation is an extremely versatile source for scattering spectroscopies in general, such as total transmission, due to its good spatial coherence, allowing the studies of spatial interference phenomena in multiple scattering.

The authors thank P. Scalia, P. Johnson, and S. Faez for stimulating discussions. This work is part of the research program of the "Stichting voor Fundamenteel Onderzoek der Materie (FOM)", which is financially supported by the "Nederlandse Organisatie voor Wetenschappelijk Onderzoek (NWO)".